ELECTRON-CLOUD EFFECTS IN THE TESLA AND CLIC POSITRON DAMPING RINGS

D. Schulte [1], R. Wanzenberg [2] *, F. Zimmermann [1]

[1] CERN, Geneva, Switzerland
[2] DESY, Hamburg, Germany

Abstract

Damping rings reduce the emittances delivered by the particle sources to the small values required for the linear collider. Electron-cloud effects in such a damping ring can cause transverse single bunch instabilities leading finally to an emittance blow up.

In this paper, the density of the electron cloud is calculated for the beam and vacuum chamber parameters of the TESLA and CLIC damping rings. The arc and the damping wiggler section are studied separately. For the TESLA dogbone ring also the electron cloud in the long straight sections is investigated. The distribution of photons incident on the vacuum chamber around either ring is simulated for various antechamber parameters, in order to estimate the local production rates of photoelectrons, which is a critical parameter for the electron build up.

From the computed final electron densities, an effective transverse single bunch wakefield due to the electron cloud is obtained and a first assessment made of the resulting single-bunch instabilities.

Both analytical estimates and numerical simulations suggest that, for the TESLA damping ring, the design bunch intensity is below the threshold of the electron-driven single-bunch instability, if the arcs and the wigglers are equipped with an antechamber intercepting 90% of the photons, if synchrotron-radiation masks or additional bending magnets are added to protect the long straights, and if the maximum secondary emission yield is $\delta_{\max} \leq 1.6$. According to the numerical simulations a special coating of the wiggler vacuum chamber by a material with a low secondary emission yield would be necessary to keep the electron cloud density below 2.0×10^{12} m^{-3}.

In the arcs of the CLIC damping ring about 99% to 99.9% of the photons need to be absorbed by antechambers, which looks possible from photon-flux simulations. For the CLIC wiggler, the antechamber absorption efficiency should be about 95% or higher and the maximum secondary yield $\delta_{\max} \leq 1.2$, in order to avoid single-bunch blow up due to the electron cloud. The results for CLIC are similar to those for the NLC/GLC damping ring [1]. The CLIC requirements may become more relaxed as the design parameters evolve towards lower bunch charges.

For TESLA and CLIC the analytical and numerical estimates of the threshold electron density for single-bunch blow up differ, which requires further studies.

* rainer.wanzenberg@desy.de

INTRODUCTION

Damping rings are necessary to reduce the emittances obtained from the particle sources to the design values of the linear collider. Emittance reduction is achieved via the process of radiation damping. The design of the damping ring has to ensure a small emittance and a sufficiently short damping time. The final extracted transverse emittance (ϵ_{ext}) is given by

$$\epsilon_{\rm ext} = \epsilon_{\rm eq} + (\epsilon_{\rm inj} - \epsilon_{\rm eq})\, \exp(-2\, T_{\rm st}/\tau_D), \qquad (1)$$

where $\epsilon_{\rm inj}$ and $\epsilon_{\rm eq}$ is the injected and the equilibrium emittance respectively, τ_D is the damping time and $T_{\rm st}$ is the storage time. The bending fields of the arcs do not provide enough damping to achieve the required low emittance: thus long wiggler magnet sections are necessary to provide the damping. The conceptual layout of the TESLA damping ring [2] and part of the CLIC injector complex [3], including the damping rings, are shown in Figs. 1 and 2. In positron storage rings electrons produced by photoemission, ionization and secondary emission accumulate in the vacuum chamber forming an "electron cloud". First observations of electron clouds, dating back to 1966 and 1977, have been reported from proton storage rings [4, 5]. Recent experimental observations have been reported from accelerators operating with high beam current and short bunch spacings like the B-factories (KEKB, PEP-II) [6, 7].

In 1995, a multi-bunch instability, seen at the KEK photon factory since the start of the positron beam operation in 1989, was explained by bunch-to-bunch coupling via electron clouds [8, 9]. The present understanding of the build-up of an electron cloud and of the effects of the cloud on the positron beam is based on computer simulations and measurements with different types of detectors. A summary is given in [10, 11, 12, 13]. The B-factories have successfully tackled electron cloud effects by using solenoids to trap the electrons near the wall of the vacuum chamber where they are reabsorbed before they can be accelerated by the positron beam. Nevertheless, electron-cloud effects are still an important design issue for the positron damping rings of a future linear collider. Quantifying electron cloud phenomena in a manner which yields reliable pre-

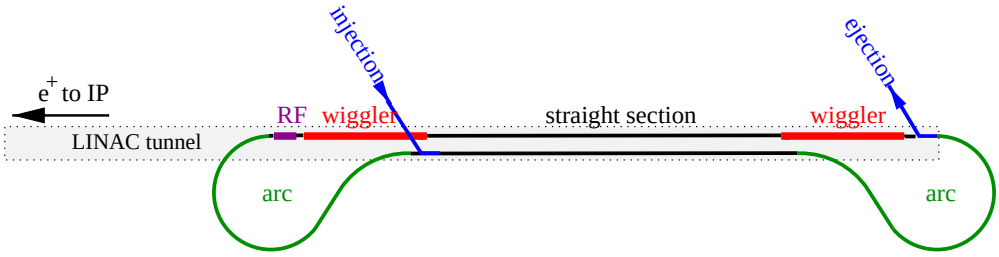

Figure 1: TESLA dogbone positron damping ring.

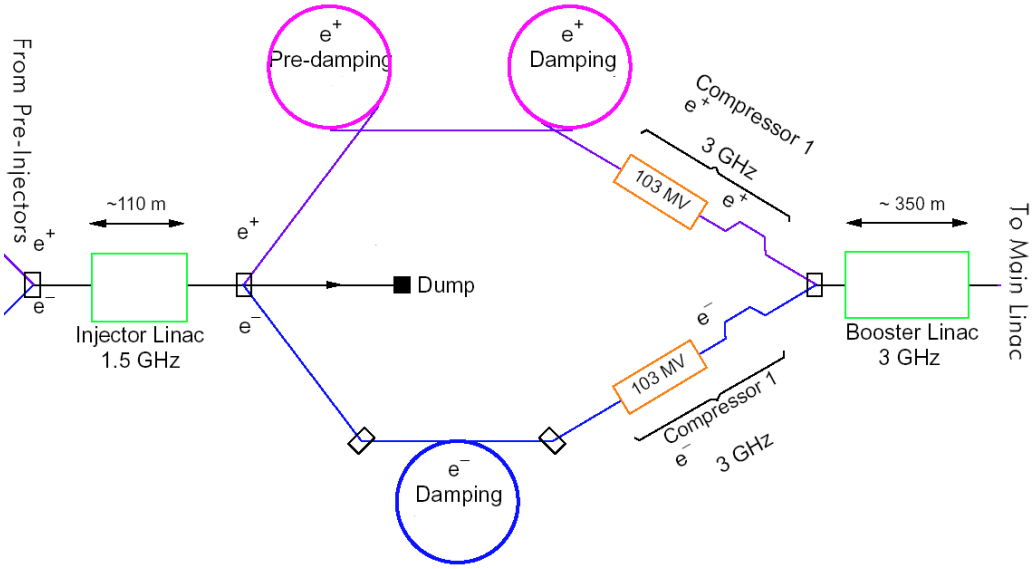

Figure 2: CLIC damping rings.

dictions for the design of new facilities is still an R&D topic. Important parameters for the build up of the electron cloud are the bunch population, the bunch spacing, the secondary electron yield of the vacuum chamber wall, and the chamber aperture. We have applied the computer code ECLOUD 2.4 [14] to study the electron cloud density for various secondary electron yields of the chamber walls. Based on these predictions for the cloud density the effects on the positron beam is estimated from an equivalent broad-band impedance model and from computer simulations with the code HEADTAIL [15].

TESLA DAMPING RING

The TESLA design is based on a 1 ms long beam pulse containing 2820 bunches, corresponding to an approximately 300 km long bunch train. To keep the damping-ring length reasonable, the bunch train has to be stored in a compressed mode with a smaller bunch spacing than in the rest of the accelerator. The damping ring length is given by the bandwidth of the injection and extraction system since each bunch has to be individually injected and ejected. A bandwidth of 50 MHz requires a ring length of 17 km. A dog bone shape is used (see Fig. 1) with mainly three sections:

- arc,
- wiggler,
- straight.

The straight section is mainly a long transport line, which connects the two arcs and the wiggler sections. Each of the three sections is considered separately with respect to electron cloud effects since the vacuum chamber dimensions and the magnetic fields are different in the three sections.

Beam parameters

The beam parameters of the TESLA positron damping ring are summarized in Table 1.

Vacuum chamber

The geometry of the vacuum chamber in the quadrupole and dipole magnets of the TESLA damping ring arc is shown in Fig. 3. The vacuum chamber in the long straight section, displayed in Fig. 4 is simply a round pipe with a diameter of 100 mm.

The chamber in the wiggler section is shown in Fig. 5 for the wiggler section and for a quadrupole corrector in the wiggler section. The computer code ECLOUD 2.4 can not handle arbitrarily shaped vacuum chambers, but it mainly considers elliptical vacuum chambers. The more complicated vacuum chambers shown in Fig. 3 and Fig. 5 have therefore been approximated as elliptical chambers with dimensions given in Table 2. Additionally several charge densities are listed in Table 2 which give first estimates for the expected electron cloud density, if one assumes that regardless of the details of the cloud build-up the electron cloud will finally neutralize the average (positron) beam charge density. First the average beam charge volume density is calculated:

$$\langle \rho_b \rangle = \frac{N_0}{A\,d}, \tag{2}$$

Table 1: TESLA damping ring parameters.

	TESLA e^+ DR		
Energy /GeV	5		
Circumference /m	17000		
revolution frequency /kHz	17.6		
Bunch Population /10^{10}	2.0		
Number of bunches	2820		
Total current /mA	160		
Bunch separation /m	5.99		
/ns	20		
Damping time / ms	28		
Invariant Emittance at injection:			
$\gamma\,\epsilon_{x,y}/10^{-6}$ m	10000		
at extraction			
$\gamma\,\epsilon_x/10^{-6}$ m	8		
$\gamma\,\epsilon_y/10^{-6}$ m	0.02		
Bunch length /mm (Equilibrium)	6		
Momentum spread			
at injection	0.5 %		
at extraction	0.13 %		
Momentum compaction α_p /10^{-4}	1.2		
Tune Q_x	72		
Q_y	44		
Q_s	0.07		
Emittance (extraction)			
ϵ_x/nm	0.818		
ϵ_y/nm	0.002		
	Arc	Straight	Wiggler
Total length /m	1900	14560	540
Bending radius /m	83.0	–	9.9
Bending field /T	0.194	–	1.63
Average beta function			
β_x /m	12.9	146.6	10.5
β_y /m	24.9	146.6	10.5
Beam size σ_x /μm	103	346	93
σ_y /μm	7	346	5
Vacuum pressure/mbar	10^{-8}	10^{-9}	10^{-8}

where N_0 is the bunch population, A is the area of the vacuum chamber cross section and d the bunch to bunch distance. For an elliptical chamber the area A is simply $\pi\,a\,b$ with the vertical and horizontal semi axes a and b of the chamber. The average bunch line charge density is N_0/d, while the bunch line charge density λ_b is

$$\lambda_b = \frac{N_0}{\sqrt{2\,\pi}\,\sigma_z}. \tag{3}$$

The neutrality volume density is defined as

$$\rho_n = \frac{N_0}{2\pi\,\sigma_x \sigma_y\,d}, \tag{4}$$

where σ_x and σ_y are the horizontal and vertical rms beam sizes. This density ρ_n is a first approximation for the max-

Table 2: Vacuum chamber dimensions and beam charge densities of TESLA Damping ring.

	TESLA DR		
	Arc	Straight	Wiggler
horizontal semi axis /mm	22	50	16
vertical semi axis /mm	18	50	9
chamber area /cm^2	12.4	78.5	5.8
Bunch Population N_0 /10^{10}	2.0	2.0	2.0
Bunch separation d/m	5.99	5.99	5.99
average bunch charge volume density$\langle\rho_b\rangle$ / (10^{12} m^{-3})	2.68	0.42	5.79
bunch line charge density λ_b/(10^{12} m^{-1})	1.33	1.33	1.33
e$^-$ neutralization density /m^{-3}	2.7×10^{12}	4.3×10^{11}	5.8×10^{12}

imum electron density within the beam, based on the assumption that the average volume charge density of the electron cloud and the positron beam inside the beam volume is finally equal (neutralization condition). An alternative definition of the neutrality would average over the entire vacuum chamber and not only over the transverse beam volume. Accordingly one can define a neutrality line density as

$$\lambda_n = 2\pi\,\sigma_x\sigma_y\;\rho_n. \tag{5}$$

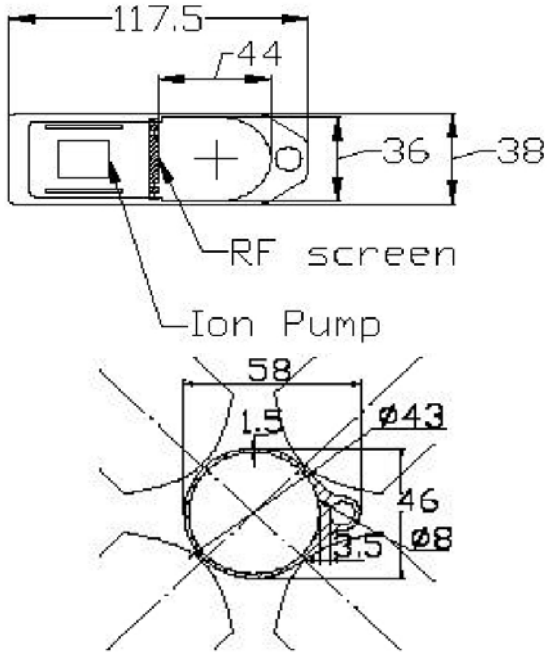

Figure 3: Vacuum chamber for dipole (top) and quadrupole (bottom) in the arc of the TESLA Damping Ring.

Photoemission and Ionization rates

A relativistic electron or positron which is bent by a magnetic field will radiate electromagnetic fields or in a quantum view will emit photons. The mean number of photons emitted per length is given as:

$$\frac{dN_\gamma}{dz} = \frac{5}{2\sqrt{3}}\,\alpha\,\frac{E}{m_e\,c^2}\,\frac{1}{\rho}, \tag{6}$$

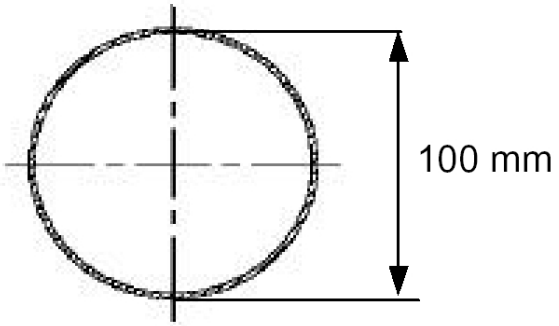

Figure 4: Vacuum chamber inside the long straight sections of the TESLA Damping Ring.

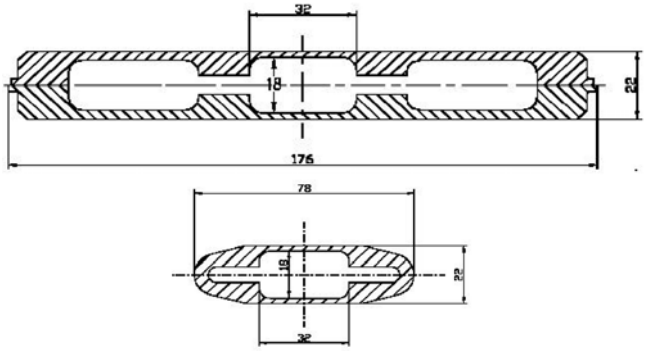

Figure 5: Vacuum chamber inside bending magnet (top) and for a quadrupole/corrector (bottom) in the wiggler section of the TESLA Damping Ring.

where E is the energy of the positron beam, m_e the rest mass of the electron, ρ the bending radius of the dipole magnet and $\alpha = e^2/(4\,\pi\,\epsilon_0\,\hbar\,c) \approx 1/137$. Photoelectrons are emitted from the chamber walls at a rate of

$$\frac{dN_{e^-}}{dz} = Y_{\rm eff}\,\frac{dN_\gamma}{dz}, \tag{7}$$

where $Y_{\rm eff}$ is the effective photoelectron emission yield. The total number of photoelectrons per length generated from one bunch is $N_0\,dN_{e^-}/dz$, where N_0 is the bunch population. The effective photoelectron emission yield depends on the photon spectrum, the photoelectric yield of the material and the photon reflectivity of the chamber.

The number of photoelectrons in the vacuum chamber will be reduced for chamber designs with an ante-chamber. A sketch of a vacuum chamber with an ante-chamber design for the arc of the TESLA damping ring is shown in Fig. 6. As a result of these unknown factors the precise value for

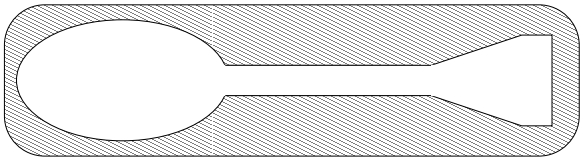

Figure 6: An alternative vacuum chamber design for the dipole in the arc of the TESLA Damping Ring. An ante-chamber is included for this option.

the effective photoelectron yield is not know. An effective photoelectron yield of 0.1 is reported for the KEK B-factory [24] vacuum chamber with no ante-chamber.

For our simulations we also take an effective photoelectron yield of

$$Y_{\rm eff} \approx 0.1 \tag{8}$$

for all simulations without an ante-chamber and and effective yield

$$Y_{\rm eff} \approx 0.01 \tag{9}$$

for vacuum chambers with an ante-chamber.

The magnetic bending strength differs significantly in the three sections of the TESLA damping ring. The resulting rough estimates of the photoemission rates are summarized for all three sections in Table 3. A more refined discussion of the photon (and hence photo-electron) distribution around the ring is presented further below. Also included in Table 3. are the ionization emission rates for the vacuum pressure of Table 1.

Table 3: Primary electron generation rates due to photoemission and ionization, in the TESLA damping ring; N_0 is the bunch population and ρ the bending radius.

	TESLA DR		
	Arc	Straight	Wiggler
N_0 /10^{10}	2.0	2.0	2.0
ρ/m	83.0	—	9.9
dN_γ/dz / m	1.242	0.0	10.38
$Y_{\rm eff}$	0.1	0.1	0.02
	(0.01)		(0.01)
dN_{e^-}/dz / m	0.124	0.0	0.2
	(0.0124)		(0.1)
$dN_{e^-}/dz^{\rm ion}$ / m	4×10^{-8}	4×10^{-9}	4×10^{-8}

CLIC DAMPING RING

The CLIC damping ring complex [3] has to provide positron and electron bunch trains with 100-Hz repetition frequency. For the positron beam the vertical emittance reduction of the pre-accelerator emittance will be a factor of about 10^7, while the horizontal emittance will be reduced by a factor of 10^5. To decouple the wide aperture requirements for the incoming positron beam from the final emittance requirements of the main linac, a collector ring with a large dynamic acceptance and relatively large equilibrium emittances is used to pre-damp the incoming beam. Then the positron beam is injected into a final damping ring with very small equilibrium emittances adapted to the main linac injection. The general layout of the electron and positron damping ring complex is shown in Fig. 2.

Beam parameters

In this paper we only consider electron cloud effects in the CLIC main damping ring. The beam parameters are summarized in Table 4 which are based on the lattice design and project target values from the year 2003 [16]. [1] At CLIC the optimum beam energy must not only be determined from optical considerations, but it also has to be chosen so as to minimize limitations from Intra-Beam Scattering (IBS).

Table 4: Parameters of the CLIC positron damping ring.

	CLIC e^+ DR	
Energy /GeV	2.424	
Circumference /m	357	
revolution frequency /kHz	839	
Bunch Population /10^{10}	0.42	
Number of bunches /train	154	
Current /train /mA	87	
Bunch separation /m	0.2	
/ns	0.667	
Damping time / ms	2.62	
Invariant Emittance		
at extraction $\gamma\,\epsilon_x/10^{-6}$ m	0.620	
$\gamma\,\epsilon_y/10^{-6}$ m	0.0087	
bunch length /mm	1.3	
Momentum spread		
at extraction	0.13%	
Momentum compaction /10^{-4}	0.731	
Tune Q_x	72	
Q_y	34	
Q_s	0.005	
Emittance (extraction) ϵ_x/nm	0.131	
ϵ_y/nm	0.002	
	Arc	Wiggler
Total length /m	197	160
Bending radius /m	8.67	4.58
Bending field /T	0.932	1.76
Average beta function		
β_x /m	1.0	4.0
β_y /m	3.0	7.0
Beam size σ_x /μm	11.4	22.8
σ_y /μm	2.3	3.5
Vacuum pressure/mbar	10^{-8}	10^{-8}

[1] Recently it is considered to change the CLIC design parameters in the following way: 385 bunches per train, bunch population $0.24\,10^{10}$, bunch spacing 0.2667 ns.

Table 5: Vacuum chamber dimensions and beam charge densities of CLIC damping ring.

	CLIC DR	
	Arc	Wiggler
horizontal semi axis /mm	22	16
vertical semi axis /mm	18	9
antechamber-slot half height		3
chamber area /cm^2	12.4	5.8
bunch population N_0 /10^{10}	0.42	0.42
bunch separation d/m	0.2	0.2
average bunch charge volume density$\langle\rho_b\rangle$ / (10^{12} m^{-3})	20.1	43.4
bunch line charge density λ_b/(10^{12} m^{-1})	1.52	1.52
e$^-$ neutralization density	1.7×10^{13} m^{-3}	3.6×10^{13} m^{-3}

Vacuum chamber

The design of the CLIC damping ring vacuum chamber has not yet been finalized. We assume that the CLIC vacuum chamber has dimensions similar to the vacuum chamber of the TESLA damping ring. A sketch of the CLIC damping ring chamber in the arc section is shown in Fig. 7. All vacuum-chamber dimensions and the beam-charge densities, computed according to Eqs. (2) and (3), are summarized in Table 5.

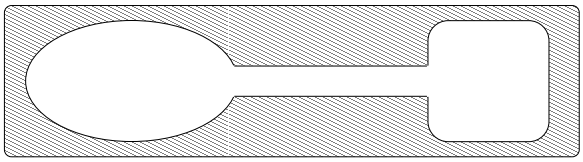

Figure 7: Vacuum chamber for the dipole in the arc of the CLIC Damping Ring.

Photoemission and Ionization rates

For a constant bending radius ρ the mean number of emitted photons and photo electrons has been calculated for the CLIC DR arc and wiggler section according to Eqs. (6) and (7). Here we have assumed that the effective photoelectron emission yield will be 0.01, taking 90% as the fraction of the photons which will be absorbed in an ante-chamber.

Table 6: Primary electron generation rates due to photoemission and ionization, in the CLIC damping ring; N_0 is the bunch population and ρ the bending radius.

	CLIC DR	
	Arc	Wiggler
N_0 /10^{10}	0.5	0.5
ρ/m	8.67	4.58
dN_γ/dz [/e^+/m]	5.764	10.903
$Y_{\rm eff}$	0.01	0.01
dN_{e^-}/dz [/e^+/m]	0.0576	0.109
$dN_{e^-}/dz^{\rm ion}$ [/$^{e^+}$/m]	4×10^{-8}	4×10^{-8}

PHOTON DISTRIBUTION

In the previous sections the photon emission rates have been estimated for a bending magnet with a constant bending radius. In this section, the code PHOTON [17, 18] is applied to the TESLA and CLIC damping-ring lattices in order to evaluate the photon distribution in detail. The PHOTON code computes the number of photons hitting the chamber wall per meter, which is an important ingredient for the simulation of the build up of an electron cloud. Also the synchrotron-radiation heat load and the average photon energy are calculated.

TESLA

In total 3.5×10^{21} photons are emitted per second, or 2.1×10^{17} per meter on average around the full circumference. The SR power per meter bend is 2760 Watt, and the total emitted power 3.2 MW. The average photon energy in the bending magnets is 2.4 keV.

The photon distribution was calculated with the code PHOTON [17, 18] for the ideal machine without orbit or optics errors. However, finite beam sizes were taken into account and, for completeness, we considered the emittances and momentum spread both at injection and at extraction. Photons were assumed to be absorbed in the wiggler antechamber, if their vertical position fell into the range of ± 3 mm from the center plane. The reflectivity of the rest of the vacuum chamber was assumed to be 80%.

Figures 8, 9, 10, and 11, show the total photon flux per meter, the photons per passing positron per meter, the synchrotron-radiation heat load, and the average photon energy, respectively, around the TESLA damping ring. Photons hitting the wiggler antechamber were considered as absorbed and did not contribute to any of these quantities. Figures 12, 13, 14, and 15 show the same quantities as Figs. 8, 9, 10, and 11, but here photons falling into the vertical range of ± 3 mm from the center plane are not taken into account anywhere around the ring. This case corresponds to the situation that a vacuum chamber design with antechamber is also used in the arcs of the damping ring (as well as in the straight sections).

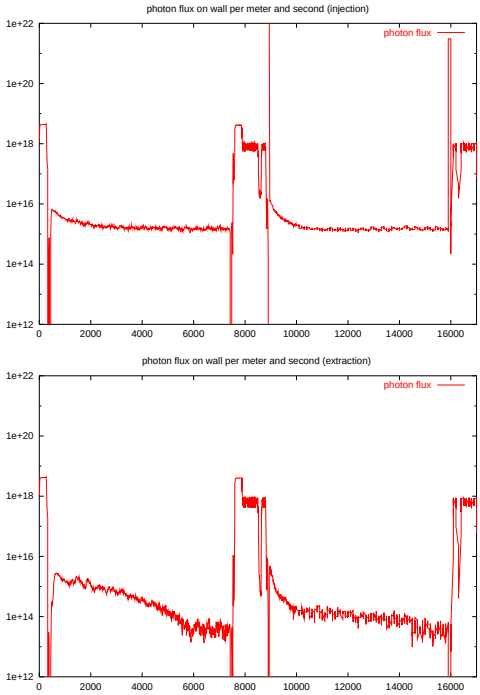

Figure 8: Photon flux on the wall of the TESLA damping ring per meter and per second for beam parameters corresponding to injection (top) and extraction (bottom), computed by PHOTON.

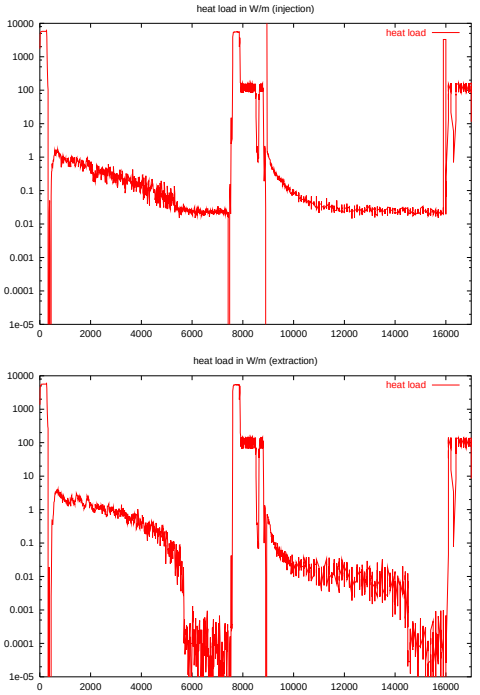

Figure 10: Synchrotron-radiation heat load on the wall of the TESLA damping ring (not counting energy absorbed in the wiggler antechamber) for beam parameters corresponding to injection (top) and extraction (bottom), computed by PHOTON.

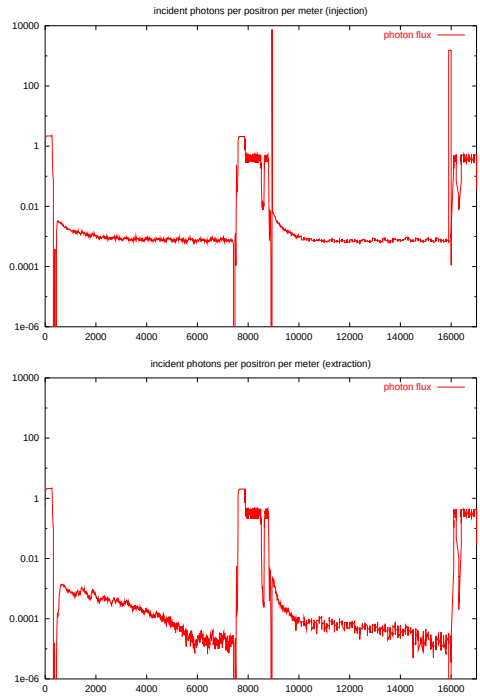

Figure 9: Photons incident on the wall of the TESLA damping ring per meter and per passing positron for beam parameters corresponding to injection (top) and extraction (bottom), computed by PHOTON.

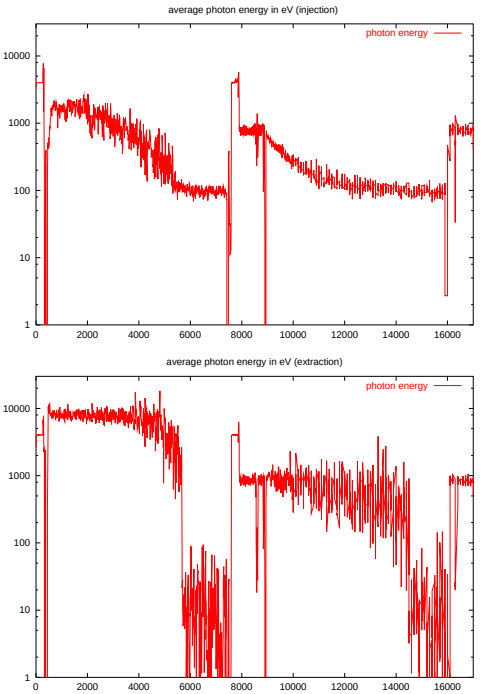

Figure 11: Average energy of photons (in eV) hitting the wall of the TESLA damping ring (not counting photons absorbed in the wiggler antechamber) for beam parameters corresponding to injection (top) and extraction (bottom), computed by PHOTON.

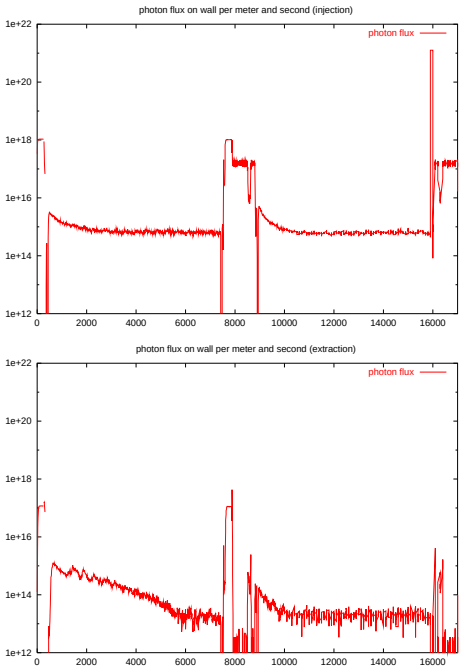

Figure 12: Photon flux on the wall of the TESLA damping ring per meter and per second for beam parameters corresponding to injection (top) and extraction (bottom), computed by PHOTON, not counting photons incident at $|y| < 3$ mm.

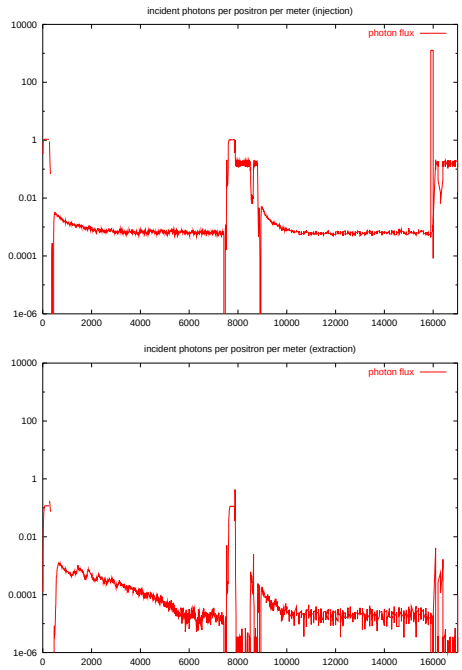

Figure 13: Photons incident on the wall of the TESLA damping ring per meter and per passing positron for beam parameters corresponding to injection (top) and extraction (bottom), computed by PHOTON, not counting photons incident at $|y| < 3$ mm.

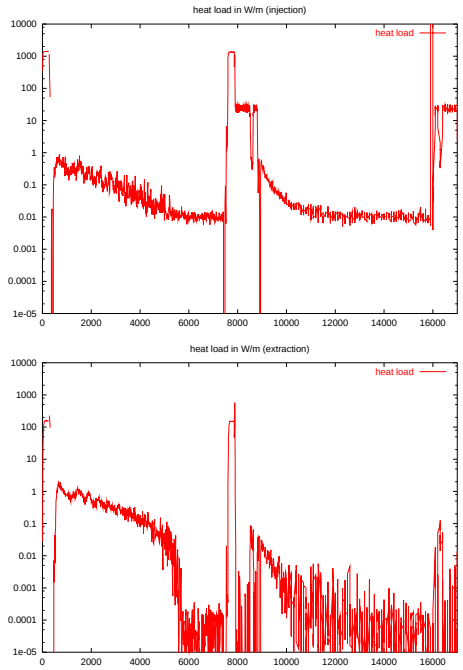

Figure 14: Synchrotron-radiation heat load on the wall of the TESLA damping ring for beam parameters corresponding to injection (top) and extraction (bottom), computed by PHOTON, not counting photons incident at $|y| < 3$ mm.

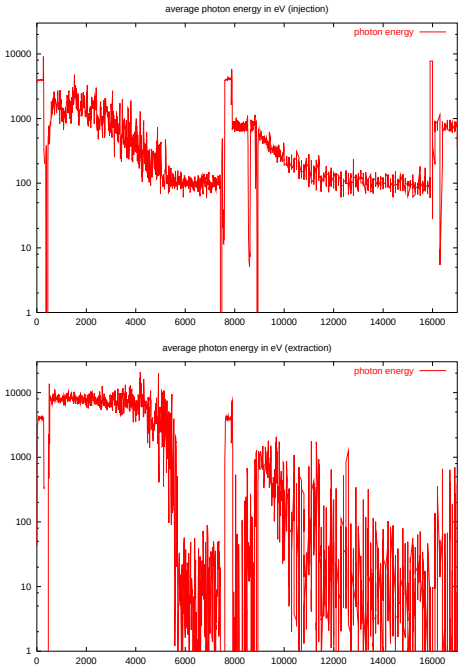

Figure 15: Average energy of photons (in eV) hitting the wall of the TESLA damping ring for beam parameters corresponding to injection (top) and extraction (bottom), computed by PHOTON, not counting photons incident at $|y| < 3$ mm.

For TESLA, from Fig. 9 with an antechamber only in the wiggler, the average rate of incident photons per meter per positron in the arcs is about 0.5 and the rate in the wiggler sections about 2 (this may be an overestimate due to a rough approximation of the antechamber location). A typical number in the straight sections is 10^{-3}. Therefore, if the straight sections are not shielded from the radiation emitted in the arcs and wigglers by a system of masks, we might expect a photoelectron yield per passing positron and meter of 10^{-4} here, in addition to the generation of ionization electrons at a much slower rate of 4×10^{-9} per positron and meter (for 10^{-9} mbar pressure).

CLIC

In total 5.9×10^{21} photons are emitted per second, or 1.6×10^{19} per meter on average around the full circumference. The SR power per meter bend is 13 kW, and the total emitted power 1.7 MW. The average photon energy in the bending magnets is 1.7 keV.

Figures 16, 17, 18, and 19 display the total photon flux per meter, the photons per passing positron per meter, the synchrotron-radiation heat load, and the average photon energy, respectively, around the CLIC damping ring. Photons hitting the wiggler antechamber were considered as absorbed and did not contribute to any of these quantities. For this set of simulations, no photons were absorbed in the arcs of the CLIC damping rings, although these will also be equipped with antechambers.

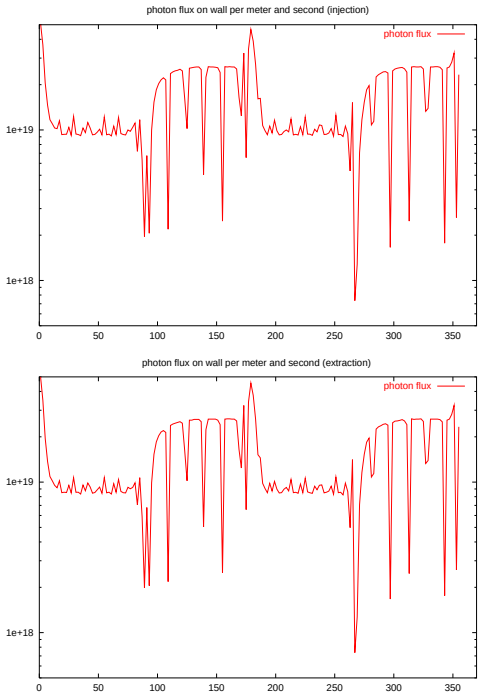

Figure 16: Photon flux on the wall of the CLIC damping ring per meter and per second for beam parameters corresponding to injection (top) and extraction (bottom), computed by PHOTON.

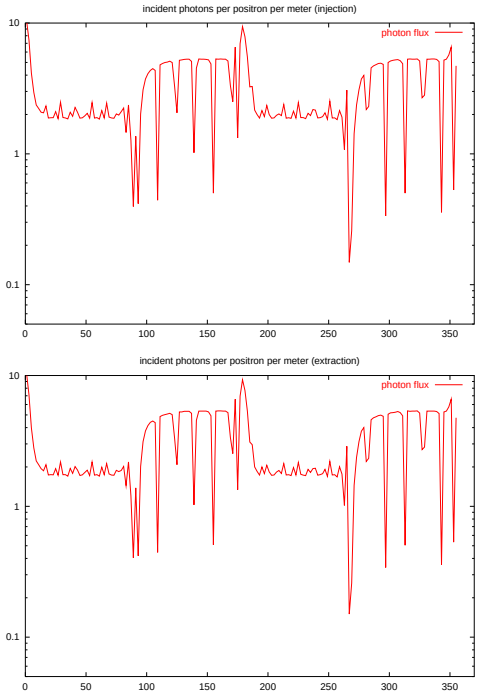

Figure 17: Photons incident on the wall of the CLIC damping ring per meter and per passing positron (not counting photons absorbed in the wiggler antechamber) for beam parameters corresponding to injection (top) and extraction (bottom), computed by PHOTON.

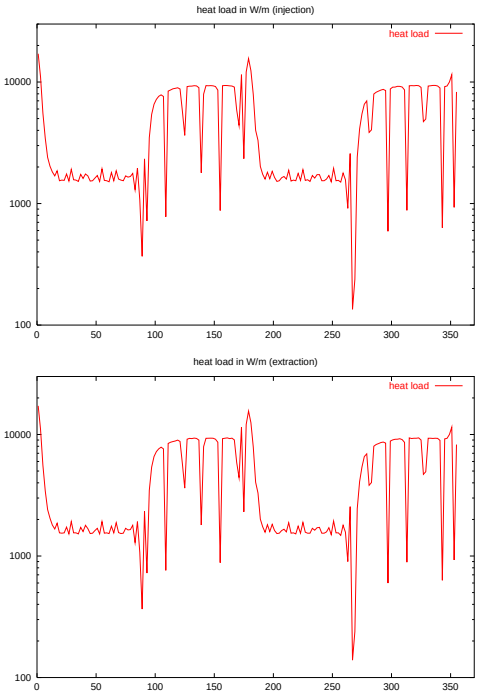

Figure 18: Synchrotron-radiation heat load on the wall of the CLIC damping ring (not counting energy absorbed in the wiggler antechamber) for beam parameters corresponding to injection (top) and extraction (bottom), computed by PHOTON; assuming an antechamber in the wiggler bends only.

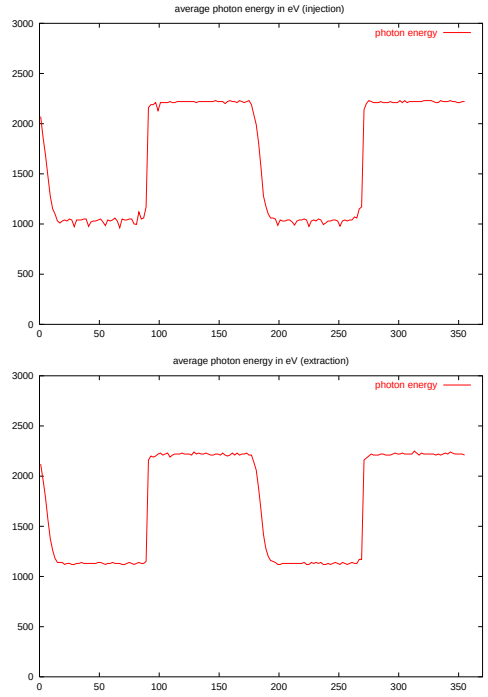

Figure 19: Average electron energy of photons hitting the wall of the CLIC damping ring (not counting photons absorbed in the wiggler antechamber) for beam parameters corresponding to injection (top) and extraction (bottom), computed by PHOTON.

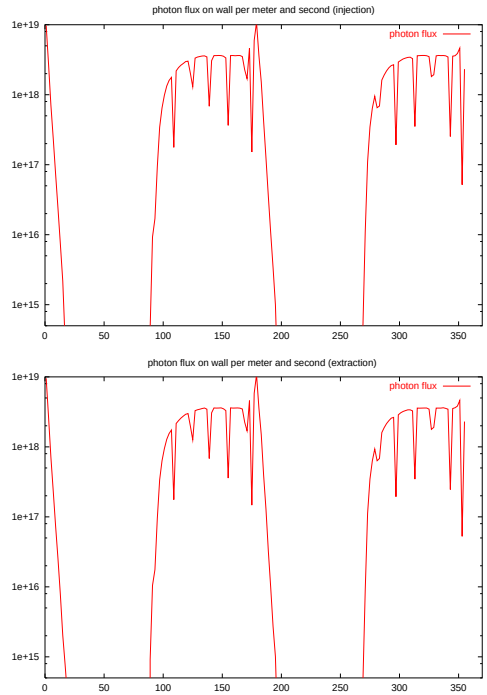

Figure 20: Photon flux on the wall of the CLIC damping ring per meter and per second for beam parameters corresponding to injection (top) and extraction (bottom), computed by PHOTON, not counting photons incident at $|y| < 3$ mm.

Figures 20, 21, 22, and 23 show the same quantities as in Figs. 16, 17, 18, and 19, but here photons falling into the vertical range of ± 3 mm from the center plane are assumed to be absorbed by antechamber, all around the ring, and are not taken into account.

For CLIC, the average rate of incident photons per meter per positron in the arcs is about 2 and the rate in the wiggler sections about 5 (again this may be an overestimate due to a rough approximation of the antechamber location). The energy of incident photons is about 1000 eV in the arcs and 2000 eV in the wigglers.

Tables 7 and 8 summarize the photoemission results estimated from the simulation for the two cases that an antechamber is present only in the bending magnets of the wigglers or that an antechamber is installed everywhere around the ring. The numbers obtained from the analytical calculation of the photoemission rate in in Tables 3 and 6 are also shown, for different hypothetical values of antechamber efficiencies.

The antechamber in the TESLA arcs has a simulated efficiency of 80%, while for the CLIC arcs the absorption efficiency exceeds 99.99%. The photon flux in the straight section of TESLA, though not exactly zero, is more than two orders of magnitude smaller than in the arcs. To completely suppress the remaining photon flux, the ring geometry would need to be changed, e.g., either by weak bending magnets behind the wigglers, or by adding synchrotron-radiation masks.

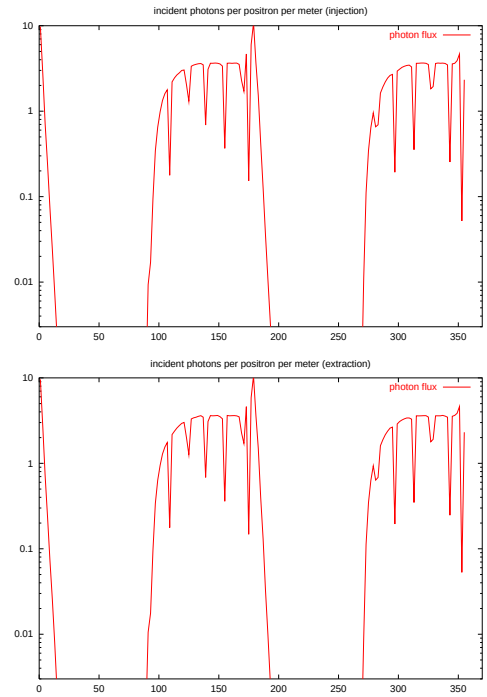

Figure 21: Photons incident on the wall of the CLIC damping ring per meter and per passing positron for beam parameters corresponding to injection (top) and extraction (bottom), computed by PHOTON, not counting photons incident at $|y| < 3$ mm.

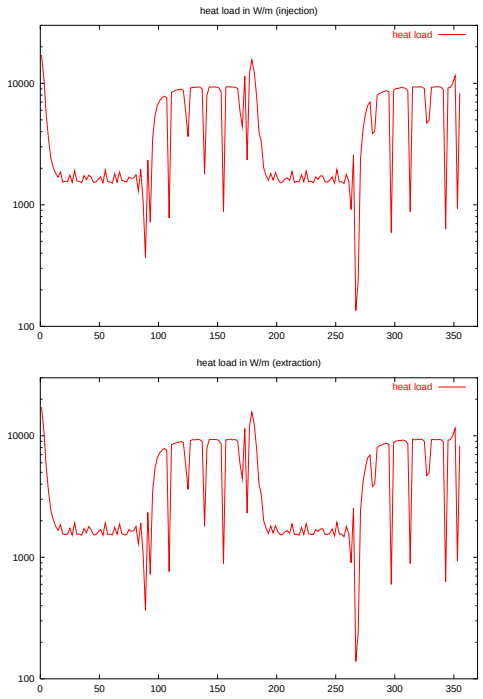

Figure 22: Synchrotron-radiation heat load on the wall of the CLIC damping ring for beam parameters corresponding to injection (top) and extraction (bottom), computed by PHOTON, not counting photons incident at $|y| < 3$ mm.

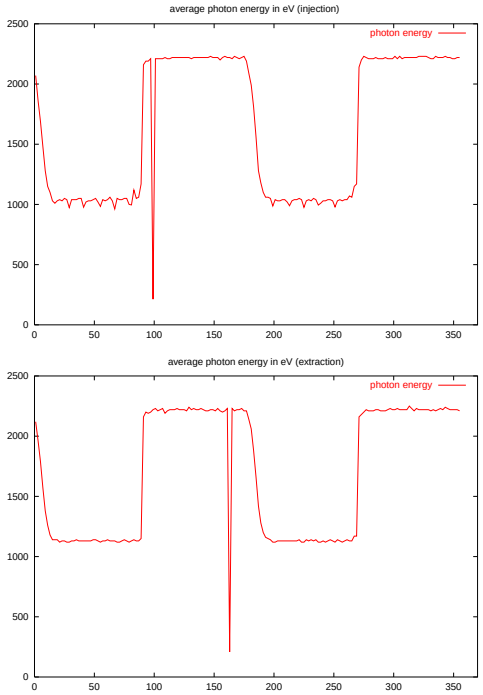

Figure 23: Average electron energy of photons hitting the wall of the CLIC damping ring for beam parameters corresponding to injection (top) and extraction (bottom), computed by PHOTON, not counting photons incident at $|y| < 3$ mm.

For the TESLA wiggler the antechamber is 90% efficient (bottom column), while for CLIC the efficiency is 85%. In summary, the efficiency of the antechamber depends on the location, and, although in some cases an efficiency far above 90% appears possible, often it is limited to 80–90%. Especially, it may be difficult to further reduce the photon flux in the long wigglers, where many photons are emitted in near-forward direction.

Table 7: Analytically estimated and simulated photoemission rate dN_{e^-}/dz in units of m^{-1} per passing positron in various sections of the TESLA damping ring, considering different configurations of antechambers, and assuming a constant photoemission yield of $Y_{\mathrm{eff}} = 0.1$ for all cases. The simulations considered a photon reflectivity of 80% outside the antechambers; the latter were treated as perfect absorbers.

	TESLA		
	Arc	Straight	Wiggler
analytical:			
no antechamber	0.124	0	1
90% protection	0.012	0	0.1
99% protection	0.001	0	0.01
simulated:			
antechamber in wiggler bends	0.05	10^{-4}	0.2
antechamber everywhere	0.02	10^{-4}	0.1

Table 8: Analytically estimated and simulated photoemission rate dN_{e^-}/dz in units of m^{-1} per passing positron in various sections of the CLIC damping ring, considering different configurations of antechambers, and assuming a constant photoemission yield of $Y_{\mathrm{eff}} = 0.1$ for all cases. The simulations considered a photon reflectivity of 80% outside the antechambers; the latter were treated as perfect absorbers.

	CLIC	
	Arc	Wiggler
analytical:		
no antechamber	0.6	2
90% protection	0.06	0.2
99% protection	0.006	0.02
simulated:		
antechamber in wiggler bends	0.2	0.5
antechamber everywhere	$< 10^{-3}$	0.3

ELECTRON CLOUD BUILD UP

The electron cloud build up in TESLA and CLIC positron damping ring was simulated using the code ECLOUD [19]. The results for the electron line density and

the central (in the beam center) electron cloud volume density are presented in separate subsections for the TESLA DR and the CLIC DR.

Electron Cloud Build Up in the TESLA DR

The electron-cloud build up has been simulated for various sections sections of the damping ring. First the results are shown for a bend and field-free region of the arc. The long straight section and the wiggler section are treated separately.

Electron Cloud Build Up in the Arcs Figures 24 and 25 show electron line densities and central volume densities for a dipole and field-free region of the arcs, assuming the maximum possible photon flux and a photoelectron emission yield of 10%. The various curves refer to different values of the maximum secondary emission yield for a constant value of $\epsilon_{\max} = 240$ eV (the primary electron energy for which the secondary yield at perpendicular incidence is maximum.) Elastically reflected low-energy electrons are included, with a reflection probability approaching 1 in the limit of zero incident energy. The electron build up appears to be dominated by the huge flux of primary photoelectrons.

To determine the beneficial effect that an antechamber might have and also to look for the threshold of beam-induced multipactoring, we repeated the same simulations with a 100-times reduced rate of photoelectrons (it is reasonable to assume that only a few percent of the photons would impact outside of an antechamber). Figures 26 and 27 show the result. The figures illustrate that the threshold for beam-induced multipactoring is around $\delta_{\max} \approx 1.6$ in the arcs, for both types of fields.

Electron Cloud Build Up in the Straight Section Figures 28 and 29 show the simulated build up for a straight section. One picture in each figure considers primary electrons due to ionization (generated inside the beam volume), the other the much larger primary rate of photoelectrons caused by reflected synchrotron light; the latter are emitted at the wall. Evidently, there is a build up by multipactoring for the larger values of $\delta_{\max}$. Fortunately there is no significant buildup-up of an electron cloud for secondary emission yields $\delta_{\max} \leq 1.6$. A secondary emission yield lower than 1.6 can easily be achieved with a copper surface after some processing time [20]. A copper plated stainless steel vacuum chamber should be used in the straight section of the TESLA damping ring. Since the primary rate of photoelectrons is dominated by photons of the reflected synchrotron light from the wiggler sections, it seems to be possible to use special photon absorbers at the end of the wiggler section to further reduce the reflected synchrotron light in the straight section.

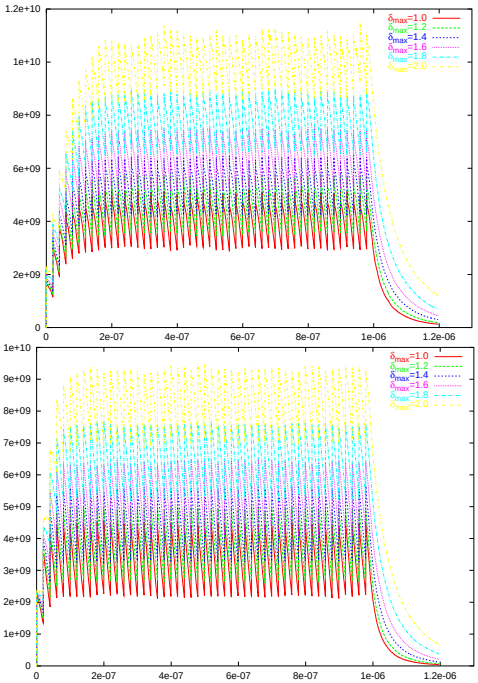

Figure 24: Electron line density in units of m^{-1} as a function of time in s for a bend (top) and a field-free region (bottom) of the arcs, assuming no antechamber ($dN_{e^-}/dz = 0.124$ photoelectrons per positron per meter); the various curves refer to 6 different values of $\delta_{\max}$.

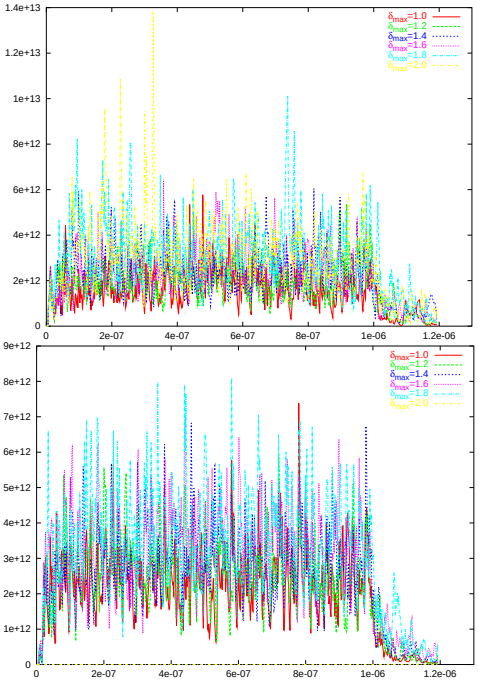

Figure 25: Central electron cloud volume density in units of m^{-3} as a function of time in s for a bend (top) and a field-free region (bottom) of the arcs, assuming no antechamber ($dN_{e^-}/dz = 0.124$ photoelectrons per positron per meter); the various curves refer to 6 different values of $\delta_{\max}$.

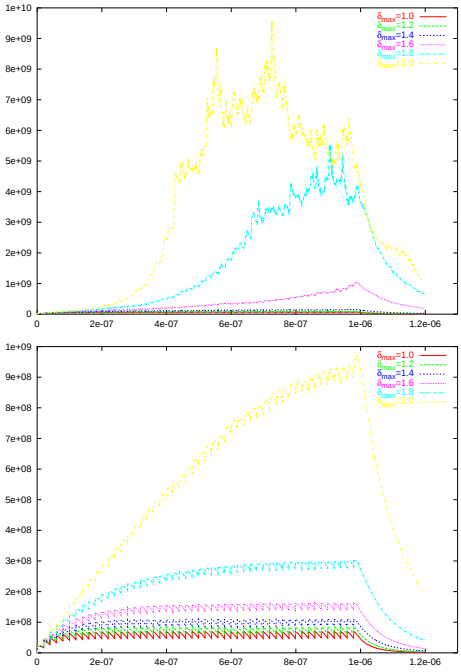

Figure 26: Electron line density in units of m^{-1} as a function of time in s for a bend (top) and a field-free region (bottom) of the arcs, assuming a reduced rate of primary photoelectrons ($dN_{e^-}/dz = 0.00124$ photoelectrons per positron per meter), possibly provided by an antechamber; the various curves refer to 6 different values of $\delta_{\max}$.

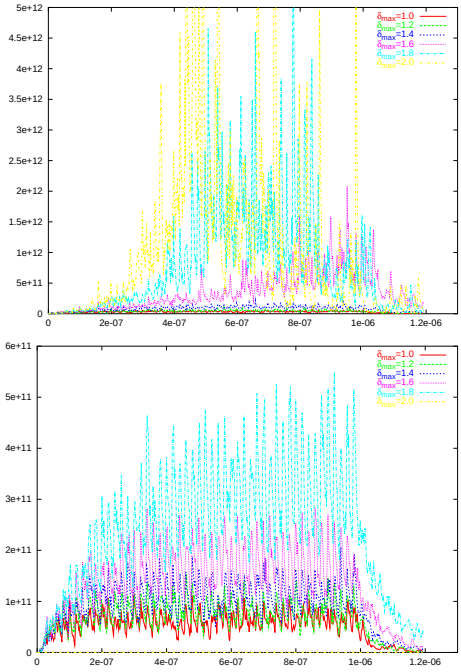

Figure 27: Central electron cloud volume density in units of m^{-3} as a function of time in s for a bend (top) and a field-free region (bottom) of the arcs, assuming a reduced rate of primary photoelectrons ($dN_{e^-}/dz = 0.00124$ photoelectrons per positron per meter), possibly provided by an antechamber; the various curves refer to 6 different values of $\delta_{\max}$.

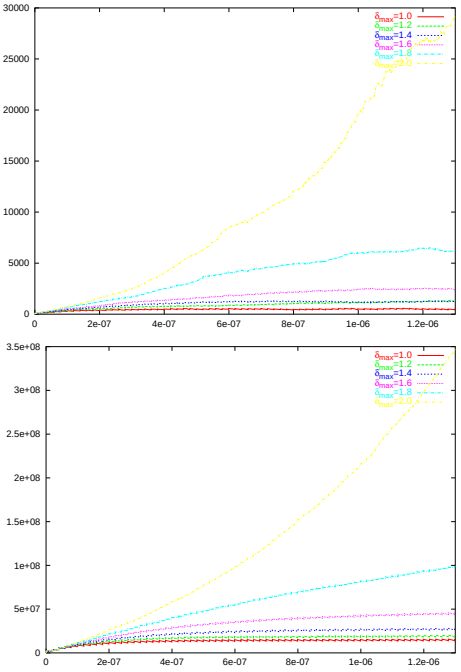

Figure 28: Electron line density in units of m^{-1} as a function of time in s for a straight section comparing the cases of primary electrons created by ionization at a rate $dN_{e^-}/dz^{\mathrm{ion}} \approx 4 \times 10^{-9}\ \mathrm{m}^{-1}$ (top) and primaries due to photoemission at a rate $dN_{e^-}/dz \approx 10^{-4}\ \mathrm{m}^{-1}$ (bottom); the various curves refer to 6 different values of $\delta_{\max}$.

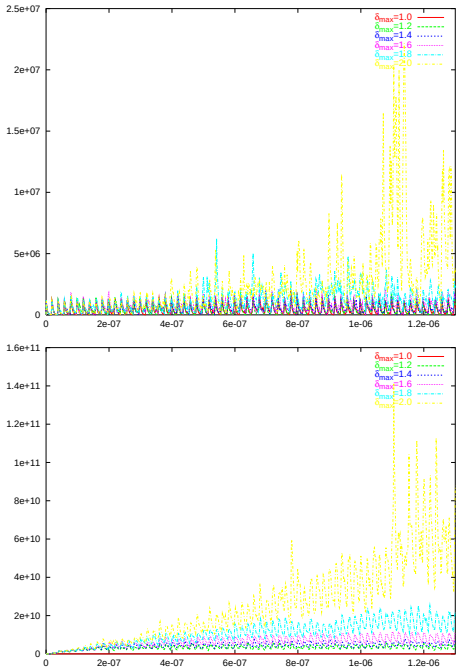

Figure 29: Electron central volume density in units of m^{-3} as a function of time in s for a straight section comparing the cases of primary electrons created by ionization at a rate $dN_{e^-}/dz^{\mathrm{ion}} \approx 4 \times 10^{-9}\ \mathrm{m}^{-1}$ (top) and primaries due to photoemission at a rate $dN_{e^-}/dz \approx 10^{-4}\ \mathrm{m}^{-1}$ (bottom); the various curves refer to 6 different values of $\delta_{\max}$.

Electron Cloud Build Up in the Wiggler Several models of the magnetic field in the wiggler sections are considered for the simulation of the build up of the electron cloud. Figure 30 shows the simulated build up in a bend with a field strength equivalent to the peak magnetic field strength of the TESLA wiggler magnet (1.68 T). The computer code ECLOUD [19] has been extended to handle also more sophisticated models of the magnetic field of a wiggler. The wiggler field can be expanded in a cylindrical mode representation [21]:

$$\begin{aligned} B_\rho &= \sum A_{mn}\, I'_m(nk_z\rho)\, \sin(m\phi)\, \cos(nk_z z) \qquad (10)\\ B_\phi &= \sum A_{mn}\, \frac{m}{nk_z\rho}\, I_m(nk_z\rho)\, \cos(m\phi)\, \cos(nk_z z)\\ B_z &= -\sum A_{mn}\, I_m(nk_z\rho)\, \sin(m\phi)\, \sin(nk_z z), \end{aligned}$$

where $I_m(x)$ are modified Bessel functions of the first kind and A_{mn} are the expansions coefficients, which are obtained from a Fourier analysis of the radial field component of the wiggler field in the azimuthal and longitudinal variables at a fixed reference radius. Figure 31 shows the simulated build up in the TESLA wiggler using a 1st order expansion of the wiggler field based on this cylindrical mode representation.

An alternative expansion of a periodic magnet system, which is commonly used for planar wiggler magnets, is based on the following expansion in Cartesian coordinates:

$$\begin{aligned} B_y &= \sum_{n\,\mathrm{odd}} B_n\, \cosh(nk_y y)\, \sin(nk_z z) \qquad (11)\\ B_z &= \sum_{n\,\mathrm{odd}} B_n\, \sinh(nk_y y)\, \cos(nk_z z), \end{aligned}$$

with $k_y = k_z$. The results from the ECLOUD code for a 1st order expansion of the wiggler field in Cartesian coordinates are shown in Fig. 32. The results for the electron line density and central electron cloud volume density for $\delta_{\max} = 1.6$ are compared in Fig. 33 for the three different models of the wiggler field (constant bend, first term in a cylindrical expansion, first term in a harmonic expansion in Cartesian coordinates). The predicted electron cloud density does not strongly depend on the model of the wiggler field. This indicate that the longitudinal field component of the magnetic field of the wiggler does not change the dynamics of the electrons in the cloud significantly. For a secondary emission yield of $\delta_{\max} = 1.6$ the simulations predict a central electron cloud volume density close to the neutralization density.

Electron Cloud Build Up in the CLIC DR

For the CLIC damping ring we consider the build up of an electron cloud in the arc and in the wiggler section of the ring. The value of the maximum secondary emission yield (assumed to occur at a constant primary energy of $\epsilon_{\max} = 240$ eV for perpendicular incidence) is varied between 1.0 and 2.0 to investigate the dependence of the electron cloud build up on the properties of the material.

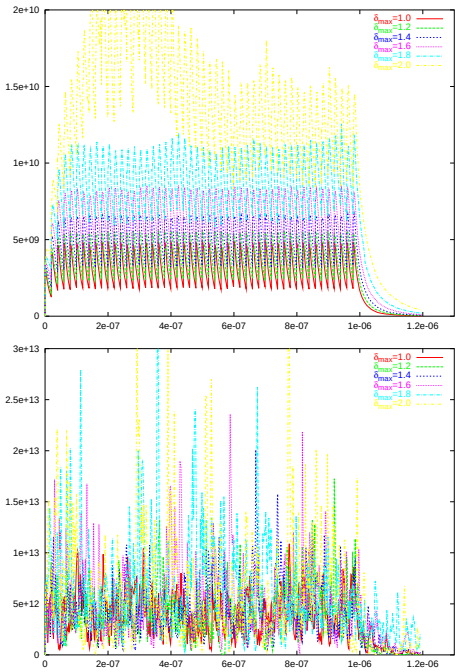

Figure 30: Electron line density (top) in units of m^{-1} and central electron cloud volume density (bottom) in units of m^{-3} as a function of time in s for a bending field whose strength is equal to the peak field of the TESLA wiggler, assuming $dN_{e^-}/dz = 0.2$ photoelectrons per positron per meter; the various curves refer to 6 different values of $\delta_{\max}$.

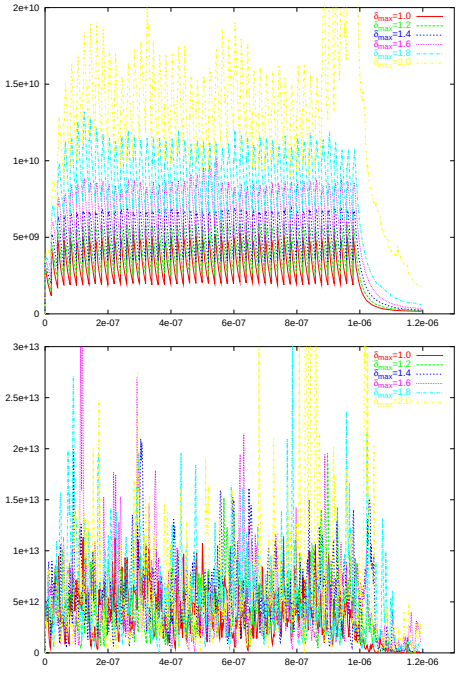

Figure 31: Electron line density (top) in units of m^{-1} and central electron cloud volume density (bottom) in units of m^{-3} as a function of time in s for a 1st order expansion of the TESLA wiggler field in cylindrical coordinates, assuming $dN_{e^-}/dz = 0.2$ photoelectrons per positron per meter; the various curves refer to 6 different values of $\delta_{\max}$.

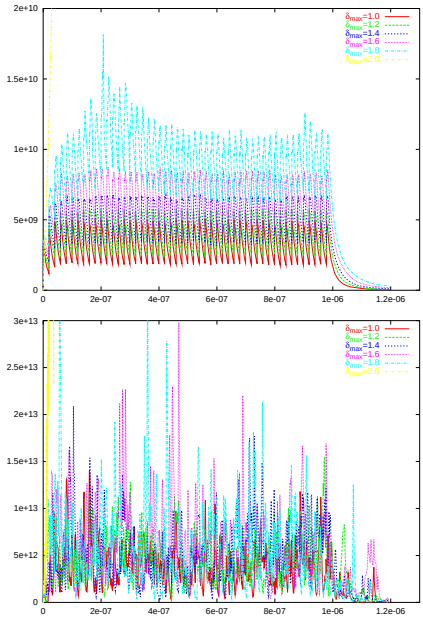

Figure 32: Electron line density (top) in units of m^{-1} and central electron cloud volume density (bottom) in units of m^{-3} as a function of time in s in a 1st order harmonic expansion of the TESLA wiggler field in Cartesian coordinates, assuming $dN_{e^-}/dz = 0.2$ photoelectrons per positron per meter; the various curves refer to 6 different values of $\delta_{\max}$.

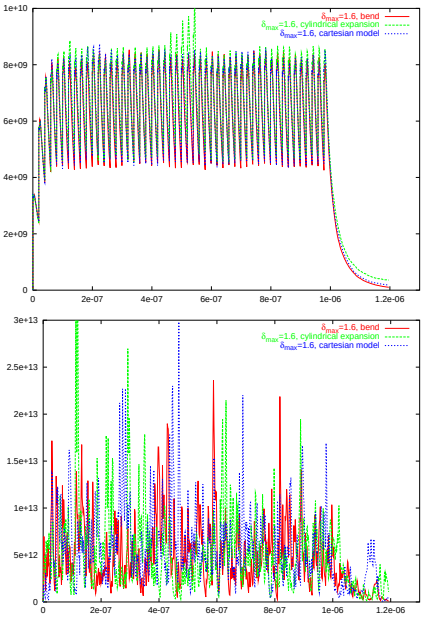

Figure 33: Electron line density (top) in units of m^{-1} and central electron cloud volume density (bottom) in units of m^{-3} as a function of time in s for $\delta_{\max} = 1.6$, comparing the three different models of the TESLA wiggler field (constant bend, first term in a cylindrical expansion, first term in a harmonic expansion), assuming $dN_{e^-}/dz = 0.2$ photoelectrons per positron per meter.

Again simulations with the code ECLOUD include elastically reflected low-energy electrons, with a reflection probability approaching 1 in the limit of zero incident energy.

Electron Cloud Build Up in the Arcs The electron line densities and central volume densities in a dipole and field-free region of the arcs are illustrated by Figures 34 and 35 for a primary electron-generation rate of about $dN_{e^-}/dz = 0.06$ photoelectrons per positron per meter (as expected with an antechamber of 90% absorption efficiency). The various curves refer to different values of the maximum secondary emission yield. The beneficial effect of an antechamber was taken into account as a 10% reduction factor in the number of incident photons, and a photoelectron emission yield per absorbed photon of also 10% was assumed, so that the primary electron rate corresponds to 1% of the emitted photon flux. The simulations with the code PHOTON (see Fig. 17) show a largest possible photon flux of about 2.0 photons per positron and meter in the arcs of the CLIC damping ring, without an arc antechamber, and (see 21) virtually zero flux when an antechamber is present. The photoelectron rate assumed here is thus rather pessimistic.

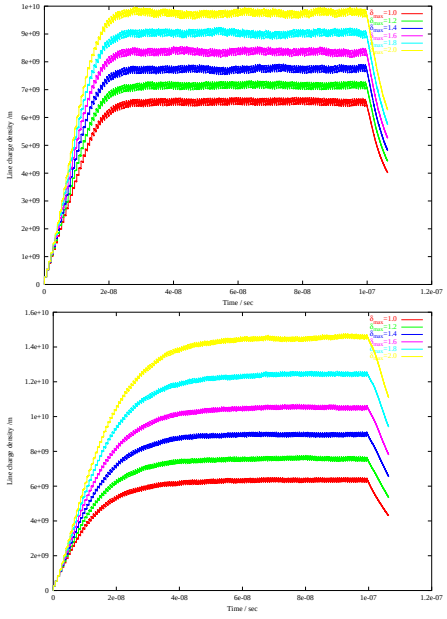

Figure 34: Electron line density in units of m^{-1} as a function of time in s for a bend (top) and a field-free region (bottom) of the CLIC arcs, assuming $dN_{e^-}/dz = 0.0576$ photoelectrons per positron per meter; the various curves refer to 6 different values of $\delta_{\max}$.

Electron Cloud Build Up in the Wiggler The magnetic field of the CLIC wiggler is modeled as a bend with a field strength equivalent to the peak magnetic field strength of the wiggler magnet (1.76 T) and in a 1st order harmonic expansion of the field in Cartesian coordinates. The results for the electron line density and central electron cloud volume density are shown in Figs. 36 and 37 for a rate of about

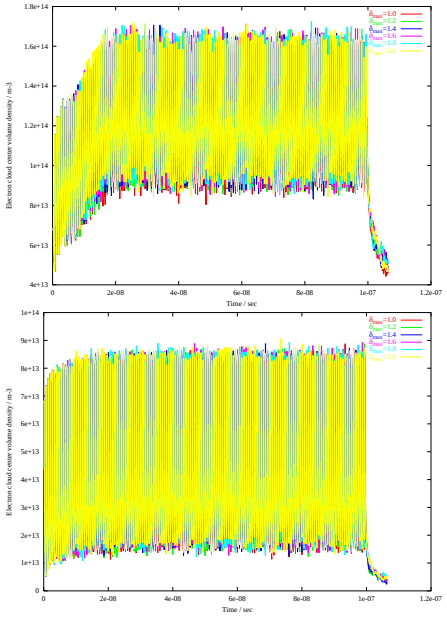

Figure 35: Central electron cloud volume density in units of m^{-3} as a function of time in s for a bend (top) and a field-free region (bottom) of the CLIC arcs, assuming $dN_{e^-}/dz = 0.0576$ photoelectrons per positron per meter; the various curves refer to 6 different values of $\delta_{\max}$.

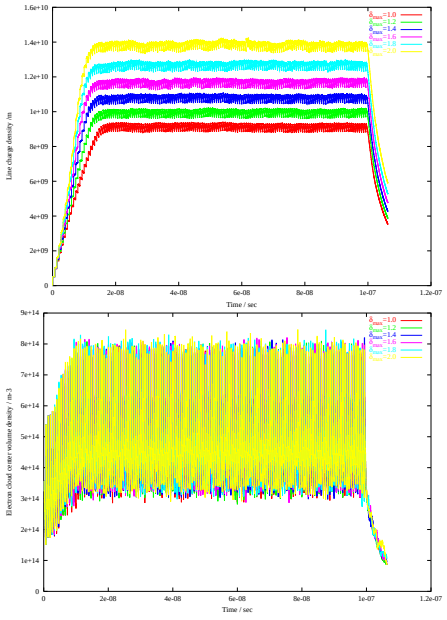

Figure 36: Electron line density (top) in units of m^{-1} and central electron cloud volume density (bottom) in units of m^{-3} as a function of time in s for a bend with a field strength equivalent to the peak magnetic field strength of the CLIC wiggler magnet (1.76 T), assuming $dN_{e^-}/dz = 0.11$ photoelectrons per positron per meter; the various curves refer to 6 different values of $\delta_{\max}$. Shown is the passage of 154 bunches followed by a gap.

$dN_{e^-}/dz = 0.11$ photoelectrons per positron per meter. Here it is assumed that 90% of the generated photons

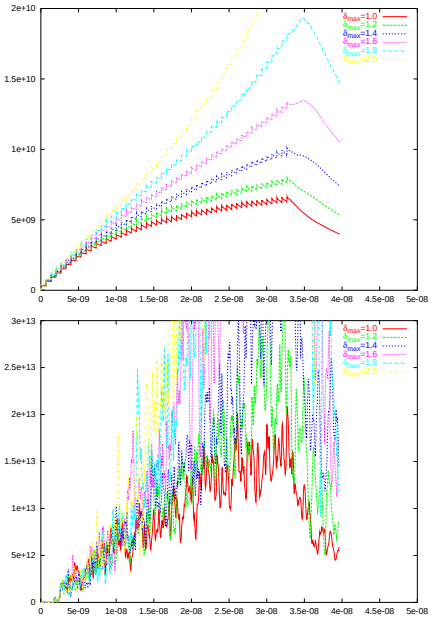

Figure 37: Electron line density (top) in units of m^{-1} and central electron cloud volume density (bottom) in units of m^{-3} as a function of time in s for a 1st order harmonic expansion of the CLIC wiggler field in Cartesian coordinates, assuming $dN_{e^-}/dz = 0.11$ photoelectrons per positron per meter; the various curves refer to 6 different values of $\delta_{\max}$. Shown is the passage of 50 bunches followed by a gap.

are absorbed in an antechamber and that the photoelectron emission yield is 10%. Unlike for the TESLA wiggler, the results for the two models differ significantly, which is not completely understood and needs further investigations in the future.

Summary of Build-Up Simulations

The electron build up in the TESLA arcs is dominated by photoemission. Densities without antechamber are of the order of $1 - 2 \times 10^{12}$ m^{-3}. If the photoemission rate is decreased by a factor 100, the arc densities are about 20 times lower than then rate without an antechamber, and the saturation values slightly depend on the maximum secondary emission yield $\delta_{\max}$. For $\delta_{\max} \leq 1.6$ there is no significant multipactoring. In the straight section the threshold $\delta_{\max}$ for multipactoring is also about 1.6. The electron density here is extremely low, 10^6 m^{-3}, if ionization electrons are the only primaries. If reflected photons are present at the level simulated by the PHOTON code, i.e., without masking or additional weak bends), the density amounts to about 5×10^9 m^{-3}. In the TESLA wiggler, the electron density again shows little dependence on $\delta_{\max}$. Simulated densities at the moment of a bunch passage are of the order 10^{12} m^{-3} assuming a photoemission rate which corresponds to the simulated effect of antechambers inside the bending magnets only. For the CLIC arcs, the simulated electron density is about 5×10^{13} m^{-3} to 10^{14} m^{-3}, if 90% of the photons are absorbed by an antechamber. For-

tunately, the PHOTON simulations suggest that the absorption efficiency for the CLIC arcs can exceed 99.9%. Since the dependence on $\delta_{\max}$ is weak, the electron cloud density in the CLIC arcs would decrease in proportion, down to values of 5×10^{11} m^{-3} or 10^{12} m^{-3}. Lastly, in the CLIC wiggler, the electron densities for $\delta_{\max} \leq 1.2$ are of the order 1.5×10^{13} assuming a 95% antechamber efficiency. The simulated antechamber efficiency is only 85%. Given the tolerance on the density determined in the following section, additional means of reducing the electron-cloud density may prove necessary. These means could include, e.g., equipping the wiggler dipoles or quadrupoles with a masking system, increasing the half height of the antechamber slits beyond the assumed value of 3 mm, or installing a system of clearing electrodes.

EMITTANCE GROWTH AND INSTABILITY

In this section we will discuss the effect of the electron cloud on the beam. First we study the pinch of the electron cloud during the passage of a positron bunch. Next, we will analyze the likelihood of head-tail instabilities using a broad-band resonator model. These results are finally compared with computer simulations.

Pinch Effect

We have simulated the electron pinch during a bunch passage, using a simple program, similar to that presented by E. Benedetto in [22]. Figures 38 and 39 show the density enhancement as a function of longitudinal position in a wiggler magnet for TESLA and CLIC, respectively. Traces of the electron oscillation frequency are visible, especially in the central density. The maximum enhancement is of the order of a factor 100 on axis.

At 1σ the density evolution is smoother and the oscillations are washed out. Analytically, the number of oscillations over $\sqrt{2\pi}\sigma_z$ is

$$n_{\rm osc} \approx \sqrt{\frac{2r_e\,N_b\,\sigma_z}{(2\pi)^{3/2}\sigma_y(\sigma_x+\sigma_y)}}\,. \qquad (12)$$

Inserting numbers for the TESLA wiggler, $\sigma_x \approx 93$ μm, $\sigma_y \approx 5$ μm, $\sigma_z \approx 6$ mm, and $N_b \approx 2\times10^{10}$ yields $n_{\rm osc} \approx 9.5$. For the CLIC wiggler, we have $\sigma_x \approx 23$ μm, $\sigma_y \approx 3.5$ μm, $\sigma z \approx 1.3$ mm, $N_b \approx 4.2\times10^{9}$, and $r_e \approx 2.818\times10^{-15}$ m, from which we compute $n_{\rm osc} \approx 10.76$. The number of oscillations inside the bunch is quite comparable for TESLA and CLIC, which may explain why the density enhancements inside the bunch are so similar.

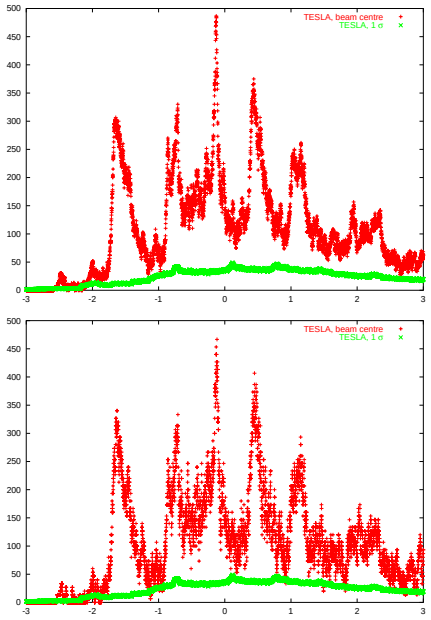

Figure 38: Enhancement of the electron cloud density at the center of the beam and on an ellipse at transverse distance 1 σ as a function of longitudinal position along the bunch in units of σ_z (the head is on the left) for TESLA. The top picture refers to a cloud size equal to 30 times the beam size, the bottom picture to one equal to 60 times the beam size.

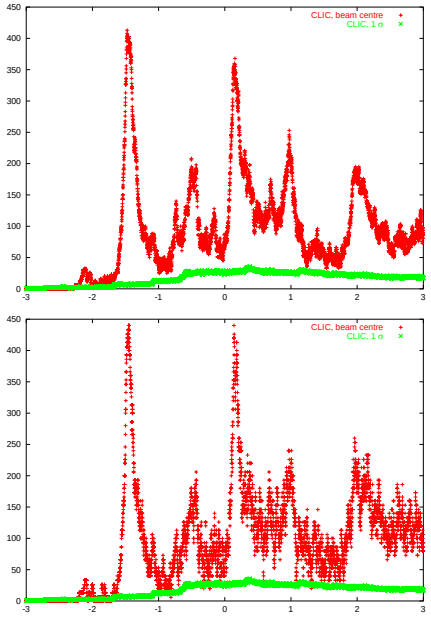

Figure 39: Enhancement of electron cloud density at the center of the beam and on an ellipse at transverse distance 1 σ as a function of longitudinal position along the bunch in units of σ_z (the head is on the left) for CLIC. The top picture refers to a cloud size equal to 30 times the beam size, the bottom picture to one equal to 60 times the beam size.

Broadband Resonator Model

In [27, 28] a broad band resonator model has been developed to estimate the effect of the electron cloud on the positron bunch. The line charge densities λ_c of the electron cloud and λ_b of the positron beam are the basic ingredients of the model, as well as the transverse beam dimensions (σ_x and σ_y). The (dipole) wake field of the broad band resonator can be written as:

$$w_1(s) = \hat{w_1}\, \sin\left(\omega_c \frac{s}{c}\right)\, \exp\left(-\frac{\omega_c}{2\,Q}\frac{s}{c}\right), \qquad (13)$$

with

$$\hat{w_1} = \frac{1}{4\,\pi\epsilon_0}\frac{\gamma}{r_e\,c^3}\,\frac{1}{\lambda_b}\,\omega_b^2\,\omega_c\,C, \qquad (14)$$

and

$$\omega_b^2 = \frac{1}{\gamma}\,\frac{r_e\,c^2}{(\sigma_x+\sigma_y)\,\sigma_y}\,\lambda_c, \qquad \omega_c^2 = \frac{r_e\,c^2}{(\sigma_x+\sigma_y)\,\sigma_y}\,\lambda_b, \qquad (15)$$

with r_e the classical electron radius, γ the beam energy measured in units of the rest mass, and C the circumference of the ring.

The dipole wake within a bunch can be calculated as the convolution integral of the point charge wake $w_1(s)$ with the Gaussian charge density in the bunch $g(s) = \exp(-\frac{1}{2}(s/\sigma_z)^2)/(\sigma_z\,\sqrt{2\,\pi})$:

$$W_1(s) = \int_0^\infty d\xi\; g(s-\xi)\; w_1(\xi). \qquad (16)$$

The "cloud" frequency ω_c is the frequency of the broad band resonator. This frequency depends only on the properties of the positron beam. A Q-value of 5 has been assumed to take into account the broad band characteristic of the impedance.

The strong-head tail instability can be treated in a simplified way using a two particle model [29]. The equations of motion during the time $0 < s/c < T_s/2$, where $T_s = 1/f_s$ is the synchrotron oscillation period, are

$$\begin{aligned} \frac{d^2}{ds^2}\,y_1 + \left(\frac{\omega_\beta(\delta_1)}{c}\right)^2\, y_1 &= 0 \\ \frac{d^2}{ds^2}\,y_2 + \left(\frac{\omega_\beta(\delta_2)}{c}\right)^2\, y_2 &= \frac{1}{m_e\,c^2\gamma}e\,q\,\frac{1}{C}\mathcal{W}_\perp\,y_1, \end{aligned} \qquad (17)$$

where y_1 and y_2 are the transverse coordinates of macroparticles 1 and 2, δ_1 and δ_2 are the relative energy deviations ($\Delta E/E$) of the macroparticles from the design energy, ω_β is the betatron oscillation frequency, q is the total bunch charge and $\mathcal{W}_\perp$ the effective dipole wake. During the time period $T_s/2 < s/c < T_s$ the equations of motion are again Eqn. (17) but with indices 1 and 2 exchanged. For the time interval $T_s < s/c < 3\,T_s/2$ Eq. (17) applies again, and so forth. The effective wake due to the head macroparticle can be approximated as the wake within the bunch at $s = \sigma_z$:

$$\mathcal{W}_\perp = W_1(\sigma_z) = \int_0^\infty d\xi\; g(\sigma_z-\xi)\; w_1(\xi), \qquad (18)$$

where w_1 is the dipole wake from the broad band impedance.

The transverse motion is stable if the trace of the total matrix which couples the motion of the head and tail particle over one synchrotron period is smaller than two, or if

$$\Upsilon < 2, \qquad (19)$$

where the parameter Υ is defined as:

$$\Upsilon = \frac{1}{m_e\,c^2\gamma}\,e^2\,N_0\,\frac{1}{C}\mathcal{W}_\perp\,\frac{\pi}{2}\,\frac{c^2}{\omega_\beta\,\omega_s}. \qquad (20)$$

Equations (20) and (19) are used to obtain an upper limit for the effective wake $\mathcal{W}_\perp$, which is then compared to the wake potential due to the electron cloud (16). The results for the TESLA and CLIC damping rings are summarized in Table 9.

Table 9: Limit for the wakefield

	TESLA	CLIC
Energy /GeV	5	2.4
Circumference /m	17000	357
N /10^{10}	2.0	0.5
Q_y	44	34
Q_s	0.07	0.004
$\mathcal{W}_{\perp\mathrm{limit}}$ / (MV/(nC m))	14.2	57.9

TESLA The broad band impedance model has first been applied to the TESLA positron damping ring. The results are presented in Table 10, first under the assumption that the cloud density is equal to the average beam density (neutrality condition) and second using the results for the center density from the computer simulations with the ECLOUD 2.4 code assuming a secondary emission yield of 1.4. The results are listed for the three sections (arc, straight, wiggler) separately. The bunch line charge density depends only on the bunch length, while the cloud frequency also depends of the transverse beam size, which differs in the various sections of the damping ring due to different focusing. The cloud frequency ω_c is measured in units of the bunch frequency

$$\omega_z = 2\,\pi\frac{c}{\sigma_z} = 314\ \mathrm{GHz} = 2\,\pi\cdot 49.9\ \mathrm{GHz} \qquad (21)$$

In the 'total' column of the table the sum of the effective wake and average of the charge density are listed. It is assumed that the cloud density has the same transverse dimensions as the beam due to the pinch effect. The line charge density of the cloud is therefore $\lambda_c = 2\,\pi\,\sigma_x\,\sigma_y\,\rho_c$, where ρ_c is the volume charge density in the center of the vacuum chamber obtained from computer simulations or calculated from the condition of neutrality.

The transverse wakefields $W_1(\sigma_z)$ due to the electron cloud is compared with the previously calculated limit from the instability threshold. Using the electron cloud charge

Table 10: Effective transverse wakefield due to the electron cloud in the TESLA positron damping ring. The results are based on estimates from the condition of neutrality and on the center density obtained from computer simulations. $W_1(\sigma_z)$ is the dipole wake potential at the position $s = \sigma_z$ in the tail of the bunch.

	TESLA DR			
	arc	straight	wiggler	total
Total length / m	1900	14560	540	17000
beam line charge density λ_b/(10^{12} m^{-1})	1.33	1.33	1.33	
cloud frequency ω_c/ω_z	2.1	0.12	2.75	
Condition of neutrality				
volume density $\langle\rho_n\rangle$ / (10^{12} m^{-3})	2.7	0.4	5.8	0.85
line charge density λ_n/(10^3 m^{-1})	12.3	318.5	15.6	274.7
$W_1(\sigma_z)_n$ / (MV/(nC m))	8.2	8.4	5.1	21.7
$W_1(\sigma_z)_n/\mathcal{W}_{\perp\mathrm{limit}}$	0.58	0.59	0.36	1.5
Simulation (SEY 1.4)				
center density / (10^{12} m^{-3})	0.7	0.01	5.8	0.27
line charge density λ_c/(10^3 m^{-1})	3.4	7.5	15.6	7.3
$W_1(\sigma_z)$ /(MV/(nC m))	2.29	0.197	5.1	7.6
$W_1(\sigma_z)/\mathcal{W}_{\perp\mathrm{limit}}$	**0.16**	**0.01**	**0.36**	**0.52**

Table 11: Effective transverse wakefield due to the electron cloud in the CLIC positron damping ring. The results are based on estimates from the condition of neutrality and on the center density obtained from computer simulations. $W_1(\sigma_z)$ is the dipole wake potential at the position $s = \sigma_z$ in the tail of the bunch.

	CLIC DR		
	arc	wiggler	total
Total length / m	197.2	160	357.2
beam line charge density λ_n/(10^{12} m^{-1})	1.52	1.52	
cloud frequency ω_c/ω_z	2.4	1.4	
Condition of neutrality			
volume density $\langle\rho_n\rangle$ / (10^{12} m^{-3})	20.1	43.4	30.5
line charge density λ_n/(10^3 m^{-1})	3.38	22.3	11.9
$W_1(\sigma_z)_n$ / (MV/(nC m))	22.6	41.7	64.2
$W_1(\sigma_z)_n/\mathcal{W}_{\perp\mathrm{limit}}$	0.39	0.72	1.11
Simulation			
center density / (10^{12} m^{-3})	10	15	209.0
line charge density λ_c/(10^3 m^{-1})	1.7	7.7	4.4
$W_1(\sigma_z)$ /(MV/(nC m))	11.3	14.4	25.7
$W_1(\sigma_z)/\mathcal{W}_{\perp\mathrm{limit}}$	**2.0**	**0.24**	**0.44**

density from the simulations it is found that the head-tail mode is stable. This two-particle model does not describe higher head-tail modes. Since the cloud frequency ω_c is larger than the bunch frequency ω_z, it cannot be excluded that higher modes could contribute to an instability.

CLIC The broad band impedance model has been also applied to the CLIC positron damping ring. The general assumption are the same as for the TESLA damping. The results, shown in Table 11, correspond to a cloud density equal to the average beam density (neutrality condition) and a density which was obtained from the computer simulations with the ECLOUD 2.4 code assuming a secondary emission yield of 1.4. The cloud frequency ω_c is measured in units of the bunch frequency, which for the CLIC damping ring is

$$\omega_z = 2\,\pi\frac{c}{\sigma_z} = 1438\ \mathrm{GHz} = 2\,\pi\cdot 228\ \mathrm{GHz}\,. \qquad (22)$$

With the assumed electron-cloud densities which amount to the simulated densities for a field-free region of the arc and for a wiggler field with $\delta_{\max} \leq 1.2$, the analytical estimate of the wake is a factor two below the instability threshold.

Simulation of Instabilities

TESLA To gain additional insight, we have performed instability simulations for TESLA with the code HEADTAIL [23], assuming that an electron cloud is built up in the wiggler section. Selected parameters are listed in Table 12. The simulated vertical single-bunch emittance growth

is shown in Fig. 40, for four different electron local densities in the wiggler. The figure illustrates that the critical density corresponding to the threshold of the (weak) instability and emittance growth in the wiggler alone is about 2×10^{12} m^{-3}, which differs significantly from the analytical estimate in Table 10.

Table 12: Parameters for TESLA instability simulations with HEADTAIL,

electron density in the wiggler	variable $1 - 6 \times 10^{12}$ m^{-3}
bunch population	2×10^{10}
hor. and vert. beta function	10.5 m
rms bunch length	6 mm
horizontal rms beam size	93 μm
vertical rms beam size	5 μm
rms momentum spread	1.3×10^{-3}
synchrotron tune	0.07
momentum compaction	0.12×10^{-3}
circumference (wiggler length)	17 km (540 m)
relativistic Lorentz factor	9785
number of electron-beam interactions / turn	5–30
hor. and vert. betatron tune	72.28, 44.18

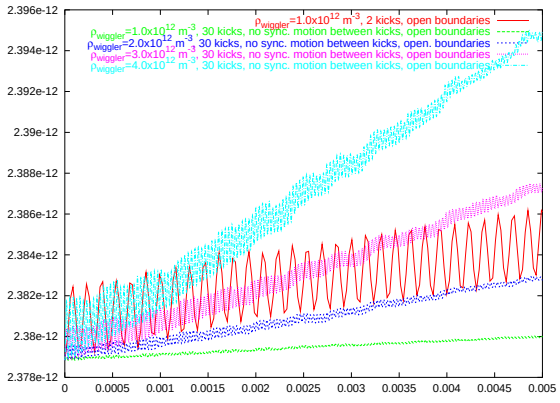

Figure 40: Vertical geometric emittance in TESLA as a function of time for various unperturbed electron-cloud densities in the wiggler without synchrotron motion between the 30 IPs applied on each turn; other parameters are listed in Table 12; open boundaries are used.

CLIC The computer code HEADTAIL [23] has also been used to simulate the instability due to the electron cloud in the CLIC damping ring. The simulated vertical single-bunch emittance growth is shown in Fig. 41, for five different electron densities in the wiggler section. Further parameters are listed in Table 13. The figure illustrates that the critical density corresponding to the threshold of the instability is about 1×10^{12} m^{-3} according to the simulations with the HEADTAIL code. This is 10 times lower than the analytical estimate.

While antechambers in the CLIC arcs will suppress the electron cloud build up to values much below the threshold, a comparison of various possible suppression schemes may be necessary for the wiggler. The available options include an increase of the antechamber-slit opening, installation of clearing electrodes, and adding radiation masks.

Why the analytical estimate do not agree with the simulations for TESLA and CLIC requires further studies.

Table 13: Parameters for CLIC instability simulations with HEADTAIL,

electron density in the wiggler	variable $0.01 - 4 \times 10^{12}$ m^{-3}
bunch population	4.2×10^{9}
hor. and vert. beta function	4, 7 m
bunch length	1.3 mm
horizontal rms beam size	23 μm
vertical rms beam size	3.5 μm
rms momentum spread	1.3×10^{-3}
synchrotron tune	0.005
momentum compaction	0.731×10^{-4}
circumference	357 m
relativistic Lorentz factor	4744
number of electron-beam interactions / turn	5–30
hor. and vert. betatron tune	72.85, 34.82

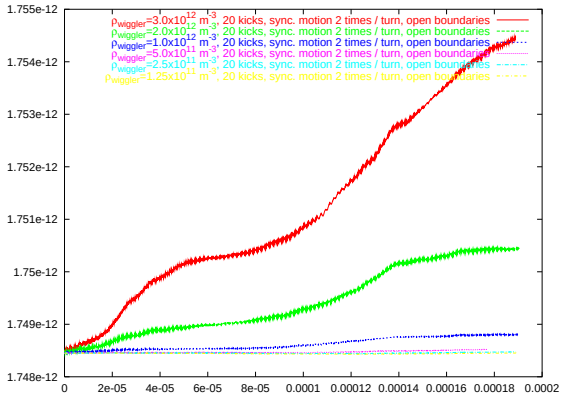

Figure 41: Vertical geometric emittance in CLIC as a function of time for different unperturbed electron-cloud densities in the wiggler for 20 electron-beam interaction points per turn; other parameters are listed in Table 13.

CONCLUSION

Electron cloud effects are an important design issue in the planning for the positron damping rings of a future linear collider. In its second report [30], the International Linear Collider Technical Review Committee has stressed the importance of further studies for all damping ring designs

to facilitate further understanding of electron clouds (chapter 9, p 470). For the TESLA and CLIC positron damping rings we have simulated the build up of an electron cloud under various conditions using the ECLOUD code. We have studied possible single bunch instabilities and emittance growth of the positron beam. For the evaluation of electron-cloud effects we have estimated the instability threshold for head-tail instabilities using a broad-band impedance model. The analytical estimate has been complemented by computer simulations using the HEADTAIL code. The computer codes had to be adapted or extended to the specific situation in the TESLA and CLIC damping rings, e.g., simulated electron build up was compared for different descriptions for the wiggler magnetic fields, the correct modeling of the one-turn synchrotron motion required some care, and various antechamber dimensions were implemented in the PHOTON code. Further studies are necessary to verify and improve the results which have been obtained here in a first assessment of the problem.

For the TESLA damping ring the build up of an electron cloud was studied for the three main sections: the arc, the long straight section and the wiggler section, separately. It was found that there is an electron cloud build up to some extent in all sections, if the design of the vacuum chamber is not improved. To cure the problems, it is necessary to ensure that the secondary emission yield is not larger than 1.4 in the arcs and the straight sections of the damping ring which means that a copper plated vacuum chamber should be used. Furthermore is it necessary to add an antechamber in the arc section of the TESLA damping ring to reduce the effective photoelectron emission yield, and to protect the long straight sections from the wiggler and arc radiation either by a masking system or additional weaker bends. The B-factories have successfully cured the electron cloud effects by using solenoids to confine the electrons near the wall of the chamber where they are absorbed by the chamber wall before the next positron bunch arrives. The above study indicates that such a measure seems not to be necessary for the TESLA damping ring. The build up of the electron cloud in the wiggler section is of some concern since local cloud densities close to the neutralization density of 5.8×10^{12} m^{-3} can occur depending on the details of the secondary emission yield and of the effectiveness of the photon absorber in the antechamber. An electron cloud density close to the neutralization density in the wiggler section is still tolerable according to the estimates of the instability threshold based on the broadband resonator model. Simulations with the code HEADTAIL show that there is a weak emittance growth when the cloud density inside the wiggler exceeds the value of about 2.0×10^{12} m^{-3}. A special coating of the wiggler vacuum chamber by a material with a low secondary emission yield would be necessary to keep the electron cloud density below that value.

The build up of an electron cloud was investigated in the arc and in the wiggler section of the CLIC damping ring. Computer simulations indicate a strong build up of an electron cloud in the arcs and, to a lesser extent, in the wiggler section. In order to keep the electron density at a tolerable level, between 99% and 99.9% of the synchrotron-radiation photons in the arcs must be absorbed in antechambers, which is possible according to the simulations. In the CLIC wiggler a maximum secondary emission yield of $\delta_{\max} \leq 1.2$ and an antechamber absorption efficiency of 95% appear to be required. Under these conditions the simulated electron density stays below the analytical threshold of the strong head-tail instability, which is about 2×10^{13} m^{-3}, averaged around the ring. A lower electron density of 10^{12} m^{-3} and hence more effort would be required to suppress a persistent (weak) emittance growth seen in the simulations, if the latter is not a numerical artifact. Possibilities are to install solenoids in the field-free regions, to add a system of clearing electrodes, or to groove the surface of the vacuum chamber [31, 32]. Presently, the CLIC design target parameters are being changed towards smaller bunch charges and shorter bunch spacings. The new parameters, once settled, will require a re-assessment of the electron-cloud effect for CLIC. As the electron energy gain acquired during a single passing bunch drops below the energy at which the secondary emission yield is maximum and far below the value required for escaping to the wall between two successive bunches, the CLIC parameters may approach a situation resembling that of a coasting beam, where no multipacting can occur.

In conclusion, we have found that some care will be required to prevent the build up of an intolerable density of electrons inside the vacuum chamber of future damping rings. Without antechambers the electron cloud is fed by a large number of photoelectrons. In the presence of antechambers the simulated densities are near the thresholds of the single-bunch instability for both the TESLA and CLIC design. A few additional countermeasures will bring the densities safely below the threshold of the head-tail instability. Our results suggest that the electron cloud does not pose a fundamental obstacle for reaching the design parameters in either TESLA or CLIC, provided that it is taken into account in the design and the appropriate remedies are implemented.

ACKNOWLEDGMENT

We would like to thank W. Decking and M. Korostelev for providing information on the TESLA and CLIC damping rings, respectively, and for many discussions. We also thank K. Ohmi, K. Oide, M. Pivi, T. Raubenheimer and A. Wolski for various helpful suggestions and comments. We acknowledge the support of the European Community - Research Infrastructure Activity under the FP6 “Structuring the European Research Area” programme CARE, contract number RII3-CT-2003-506395.

REFERENCES

[1] K. Ohmi, *Electron Cloud Effect in Damping Rings of Linear Colliders*, these proceedings.

[2] R. Brinkmann, K. Flöttmann, J. Rossbach, P. Schmüser, N. Walker, H. Weise, eds. *TESLA – Technical Design Report, Part II, The Accelerator* DESY 2001-011, ECFA 2001-209, TESLA Report 2001-23, TESLA-FEL 2001-05, March 2001

[3] The CLIC Study Team, Editor: G. Guignard, *A 3 TeV e^+ e^- Linear Collider based on CLIC Technology*, CERN 2000-008, PS Division, July 2000

[4] G. Budker, G. Dimov, V. Dudnikov, *Experiments on production of intense proton beam by charge exchange injection method*; Proceedings of the International Symposium on Electron and Positron Storage Rings, Saclay, France, VIII, 6.1 (1966)

[5] O. Gröbner, *Bunch induced multipactoring*, Proceedings of 10th Int. Conf. on High Energy Acc., Protvino (1977) 277

[6] H. Fukuma, *Electron cloud effects at KEKB*, Proc. of ECLOUD'02: Mini-Workshop on Electron-Cloud Simulations for Proton and Positron Beams, CERN, Geneva, April 2002.

[7] Kulikov et al., *The electron cloud instability at PEP II* Proceedings PAC 2001, Particle Accelerator Conference, Chicago, June, 2001

[8] K. Ohmi, *Beam and photoelectron interactions in positron storage rings*, Phys. Rev. Lett. **75** (1995) 1526

[9] M. Izawa, Y. Sato, T. Toyomasu, *The vertical instability in a positron bunched beam*, Phys. Rev. Lett. **74** (1995) 5044

[10] F. Zimmermann, *The Electron Cloud Instability: Summary of Measurements and Understanding*, Proc. of IEEE Particle Accelerator Conference (PAC 2001), Chicago, 2001

[11] F. Zimmermann et al., *Present understanding of electron cloud effects in the Large Hadron Collider*, Proceedings PAC 2003, Particle Accelerator Conference, Portland, May 12-16, 2003

[12] M.A. Furman, *Formation and Dissipation of the Electron Cloud*, Proceedings PAC 2003, Particle Accelerator Conference, Portland, May 12-16, 2003

[13] K.C. Harkay, R.A. Rosenberg, *Properties of the electron cloud in a high-energy positron and electron storage ring*, Phys. Rev. ST Accel. Beams **6**, 034402 (2003)

[14] F. Zimmermann, G. Rumolo, *Electron-Cloud Simulations: Build-Up and Related Effects*, Proc. of ECLOUD'02: Mini-Workshop on Electron-Cloud Simulations for Proton and Positron Beams, CERN, Geneva, April 2002.

[15] G. Rumolo, F. Zimmermann, *Electron-Cloud Simulations: Beam Instabilities and Wake Fields*, Proc. of ECLOUD'02: Mini-Workshop on Electron-Cloud Simulations for Proton and Positron Beams, CERN, Geneva, April 2002.

[16] M. Korostelev, F. Zimmermann, *A Lattice Design for the CLIC Damping Ring*, 26th ICFA Beam Dynamics workshop on Nanometer-Size Colliding Beams, Sep. 2-6,2002, Lausanne, CERN-Proceedings-2003-001 (2003).

[17] F. Zimmermann, *Synchrotron Radiation in the LHC Arcs – Monte-Carlo Approach*, CERN LHC Project Note 237 (2000).

[18] F. Zimmermann, A. Rossi, *Synchrotron Radiation in the LHC Experimental Insertions*, LHC Project Report 675 (2003).

[19] G. Rumolo, F. Zimmermann, *Practical User Guide for ECloud*, CERN-SL-Note-2002-016 AP (2002).

[20] J.M. Jiménez et al., *Electron Cloud with LHC-Type Beams in the SPS: A Review of Three Years of Measurements*, LHC Project Report 632 (2002).

[21] M. Pivi, private communication (2004); see also A. Wolski, *Symplectic Integrators for Nonlinear Wiggler Fields*, LCC-0062 (2001).

[22] E. Benedetto, *Analysis of the electron pinch during a bunch passage*, these proceedings

[23] G. Rumolo, F. Zimmermann, *Practical User Guide for HEADTAIL*, CERN-SL-Note-2002-036 AP (2002).

[24] K. Ohmi, *Electron cloud effect in the damping ring of Japan Linear Collider*, Proc. of ECLOUD'02: Mini-Workshop on Electron-Cloud Simulations for Proton and Positron Beams, CERN, Geneva, April 2002.

[25] N. Hilleret et al., *Secondary electron emission data for the simulation of electron cloud*, Proc. of ECLOUD'02: Mini-Workshop on Electron-Cloud Simulations for Proton and Positron Beams, CERN, Geneva, April 2002.

[26] N. Hilleret et al., *The secondary electron yield of technical materials and its variation with surface treatments*, 7th European Particle Accelerator Conference, EPAC 2000, Vienna, Austria , 26 - 30 Jun 2000

[27] K. Ohmi, F. Zimmermann, *Study of head-tail effect caused by electron cloud*, 7th European Particle Accelerator Conference, EPAC 2000, Vienna, Austria, 26 - 30 Jun 2000

[28] K. Ohmi, F. Zimmermann, E. Perevedentsev, *Wake-Field And Fast Head - Tail Instability Caused By An Electron Cloud* , Phys. Rev. E **65** (2002) 016502.

[29] R. D. Kohaupt, *Simplified presentation of head tail turbulence*, Internal Report, DESY M-80/19, Oct. 1980

[30] International Linear Collider Technical Review Committee Second Report 2003, SLAC-R-606

[31] A. Krasnov, *Molecular Pumping Properties of the LHC Arc Beam Pipe and Effective Secondary Electron Emission from a Cu Surface with Artificial Roughness*, CERN-LHC-Project-Report-671 (2003).

[32] G. Stupakov, M. Pivi, these proceedings.